Four-Phonon Scattering and Wave-Like Phonon Tunneling Drive Glassy Ultralow Lattice Thermal Conductivity in $Cs_2AgInCl_6$

Rongrong Ma(马荣荣)[1], Xiaoxiao Zhang(张笑笑)[1], Shiqi Guo(郭世祺)[1], Mei Ge(葛梅)[2], Junfeng Zhang(张均锋)[2*], and Jiangjiang Ma(马江将)[1*]

[1]*School of Physics and Electronic Engineering, Shanxi Normal University, Taiyuan 030031, China*
[2]*School of Physics and Electronic Engineering, Hainan Normal University, Haikou 571158, China*

(Received 26 May 2025; accepted manuscript online 30 July 2025)

Lead-free halide double perovskites (HDPs) provide a promising platform for high-performance thermoelectric due to their intrinsically ultralow lattice thermal conductivity κ_l. In this study, we comprehensively investigate the lattice dynamics of $Cs_2AgInCl_6$ using first-principles calculations. By explicitly incorporating four-phonon scattering and wave-like phonon tunneling, we predict a κ_l of $0.52\,W{\cdot}m^{-1}{\cdot}K^{-1}$ with a remarkably weak temperature dependence ($\kappa_l \propto T^{-0.31}$), confirming the intrinsically glass-like ultralow κ_l in $Cs_2AgInCl_6$. Further analyses reveal that hierarchical chemical bonds, loosely bonded rattling atoms and a mixed crystalline-liquid state collectively induce strong anharmonicity manifested in flat phonon modes. These factors dominate the glass-like thermal transport component of κ_l. This work uncovers the underlying mechanisms governing the unusual thermal transport properties in lead-free HDPs and offers guiding principles for designing novel energy conversion technologies.

DOI: 10.1088/0256-307X/42/9/090709 CSTR: 32039.14.0256-307X.42.9.090709

1. Introduction. The search for materials exhibiting ultralow lattice thermal conductivity κ_l is a central focus in materials science, driven by their critical applications in thermoelectric energy conversion, thermal barrier coatings, and thermal management of electronic devices.[1–4] Extrinsic approaches, like defect engineering,[5,6] nanostructuring,[7–9] and interface design,[10–13] can indeed enhance phonon scattering and suppress κ_l. However, these strategies inadvertently interfere with electronic transport, undermining charge carrier mobility. Consequently, there is a growing interest in discovering materials with intrinsically low κ_l.

The recently proposed lead-free halide double perovskites (HDPs) with the general formula $A_2B'B''X_6$ (A = Cs^+, $CH_3NH_3{}^+$; B′ = Ag^+, Na^+, Cu^+; B″ = In^{3+}, Bi^{3+}, Sb^{3+}; X = Cl^-, Br^-, I^-) have attracted considerable attention owing to their intrinsically ultralow κ_l.[14–16] HDPs exhibit superior thermal and moisture stability compared to lead-based analogues.[17,18] Moreover, the ordered B′ and B″ cation arrangement enables broad compositional tunability for precise thermal property optimization. Recent studies have shown that HDPs exhibit a glass-like temperature dependence of ultralow κ_l, such as $Cs_2AgBiBr_6$,[19] $Cs_2NaInCl_6$,[15] $Cs_2NaYbCl_6$,[14] where wave-like phonon tunneling dominates thermal transport. This behavior challenges classical phonon-transport theory, which predicts a $\kappa(T) \propto T^{-\alpha}$ ($\alpha \geq 1$) based on increasing phonon–phonon scattering with temperature. Understanding the anomalous κ_l mechanism in HDPs is therefore crucial for their identification and optimization.

This study systematically investigates lattice thermal transport properties in $Cs_2AgInCl_6$ using first-principles simulations incorporating four-phonon (4ph) scattering and wave-like tunneling effects. $Cs_2AgInCl_6$, a prototypical HDP synthesized in prior work,[20] exhibits exceptional thermal stability and a wide bandgap of 3.2 eV at room temperature.[21] Our research indicates that the κ_l of $Cs_2AgInCl_6$ is theoretically predicated to be as low as $0.52\,W{\cdot}m^{-1}{\cdot}K^{-1}$ at 300 K and exhibits a glass-like temperature dependence of $T^{-0.31}$. Calculations reveal that 4ph interactions reduce particle-like thermal conductivity κ_p by ∼35% compared to three-phonon (3ph)-only models through enhanced phonon scattering and lifetime reduction. Remarkably, wave-like tunneling dominates thermal transport at elevated temperatures, contributing 75% of κ_l at 700 K. Our analysis demonstrates that the observed glassy ultralow κ_l in $Cs_2AgInCl_6$ arises from a combination of strong chemical bond hierarchy, rattling atom vibrations, and a mixed crystalline-liquid state.

2. Methods. Electronic structure calculations based on density functional theory were performed using the Vienna *ab initio* simulation package (VASP),[22] employing the Perdew–Burke–Ernzerhof (PBE) for solids (PBEsol) exchange-correlation functional[23] under the generalized gradient approximation.[24] The phonon dispersion and harmonic interatomic force constants (IFCs) were calculated via the Phonopy package.[25] Third- and fourth-order anharmonic IFCs were extracted via the compressive sensing lattice dynamics approach.[26] The lattice thermal conductivity and relevant phonon properties were evaluated by solving the phonon Boltzmann transport equation (BTE) using the FourPhonon module of ShengBTE.[27,28]

*Corresponding authors. Email: zhangjf@hainnu.edu.cn; majiangjiang@sxnu.edu.cn
© 2025 Chinese Physical Society and IOP Publishing Ltd. All rights, including for text and data mining, AI training, and similar technologies, are reserved.

According to the Wigner transport equation as derived from the Wigner phase-space formulation of quantum mechanics,[29–31] the thermal conductivity $\kappa_{\rm l}$ includes the solid-like conductivity $\kappa_{\rm p}$ arising from particle-like phonon propagation and glass-like conductivity $\kappa_{\rm c}$ resulting from wave-like phonon tunneling, which can be expressed as

$$\kappa_{\rm l} = \kappa_{\rm p} + \kappa_{\rm c}, \tag{1}$$

where $\kappa_{\rm p}$ can be obtained from the diagonal ($s = s'$) term of the Wigner heat-flux operator,

$$\kappa_{\rm p} = \frac{1}{VN_{\rm q}} \sum_{qs} C_q^s v_q^s v_q^s \tau_q^s, \tag{2}$$

and $\kappa_{\rm c}$ is from off-diagonal ($s \neq s'$) terms,[32]

$$\kappa_{\rm c} = \frac{\hbar^2}{k_{\rm B} T^2 V N_{\rm q}} \sum_{q} \sum_{s \neq s'} \frac{\omega_q^s + \omega_q^{s'}}{2} v_q^{ss'} v_q^{ss'} \times \frac{\omega_q^s n_q^s (n_q^s + 1) + \omega_q^{s'} n_q^{s'} (n_q^{s'} + 1)}{4(\omega_q^s - \omega_q^{s'})^2 + (\Gamma_q^s + \Gamma_q^{s'})^2} (\Gamma_q^s + \Gamma_q^{s'}), \tag{3}$$

where V, $N_{\rm q}$, C_q^s, v_q^s, τ_q^s, and ω_q^s denote the primitive-cell volume, the wave-vector number in the Brillouin zone, the heat capacity, phonon group velocity, phonon lifetime, and phonon frequency for mode q and s, respectively. $\hbar$ and $k_{\rm B}$ denote Plank constant and Boltzmann constant. $v_q^{ss'}$ is the generalized interbranch phonon group velocity.[33] Γ_q^s ($\tau_q^s = 1/\Gamma_q^s$) stands for the scattering rates including 3ph, 4ph and isotope-phonon interactions.[34,35] $n_q^s = [{\rm e}^{(\hbar\omega_q^s/k_{\rm B}T)} - 1]^{-1}$ represents the equilibrium Bose–Einstein distribution. Other technical details and parameter settings are provided in the Supplementary Materials (SM).

3. Results and Discussion. $Cs_2AgInCl_6$ is a lead-free HDP that crystallizes in a face-centered cubic structure with the space group $Fm\bar{3}m$ (No. 225). It can be regarded as a modification of the standard ABX_3 cubic halide perovskites, where the B cations are orderly replaced by Ag^+ and In^{3+} ions, forming an $A_2B'B''X_6$ elpasolite structure.[37] Figures 1(a) and 1(b) show schematic diagrams of the primitive and conventional cells, generated using the visualization software VESTA.[38] The Cs, In, and Ag atoms occupy Wyckoff positions 8*c* (0.25, 0.25, 0.25), 4*a* (0, 0, 0), and 4*b* (0.50, 0.50, 0.50), respectively, while the Cl atoms reside at position 24*e* (0.24, 0, 0) at equilibrium. In $Cs_2AgInCl_6$, $[AgCl_6]$ and $[InCl_6]$ octahedra alternate in a corner-sharing arrangement with Cs^+ ions occupying the interstitial spaces. The optimized lattice constants obtained using the PBE and PBEsol functionals are listed in Table 1,

Table 1. Calculated lattice constants of $Cs_2AgInCl_6$ by using different Methods.

Approach	EXP[20]	EXP[21]	LDA[36]	PBE	PBEsol
Lattice constant (Å)	10.467	10.479	10.193	10.680	10.408

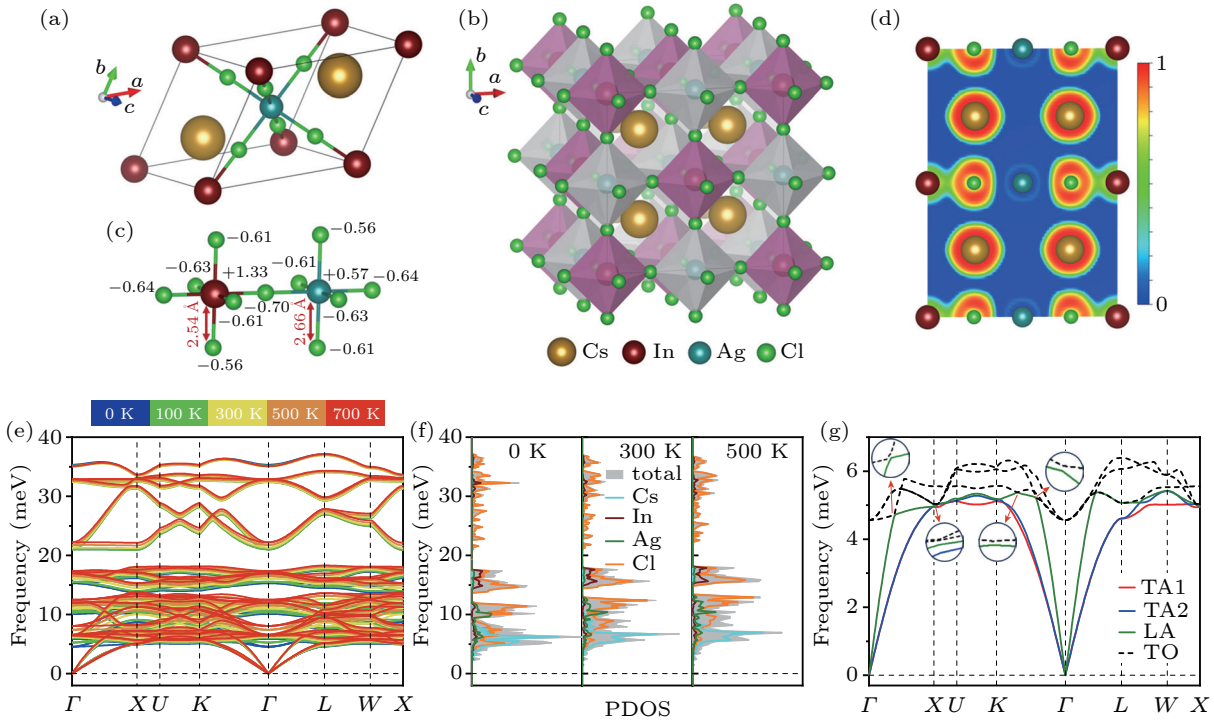

Fig. 1. The crystal structure of (a) the primitive cell and (b) a 40-atom conventional cubic cell for $Cs_2AgInCl_6$. The color code is as follows: Cs: gold, In: crimson, Ag: teal, and Cl: green. (c) $[InCl_6]$ and $[AgCl_6]$ octahedra. Bader effective charges of each atom and In-Cl and Ag-Cl bond lengths are labeled. (d) Calculated ELF of $Cs_2AgInCl_6$ along the $(-1\ -1\ 0)$ plane. The scale bar for the ELF is shown on the right. (e) The calculated phonon dispersion relations along high symmetry directions at different temperatures, where 0 K represents the result of harmonic approximation. (f) The calculated atom-projected partial and total phonon densities of states at $T = 0$, 300, and 500 K, respectively. (g) The dispersion curves of acoustic modes and three low-lying optical modes.

alongside experimental values[20,21] and local density approximation (LDA) computational results.[36] The calculated results indicate that the optimized lattice parameter obtained with the PBEsol functional shows the closest agreement with the experimental data. Notably, the octahedra in $Cs_2AgInCl_6$ exhibit a local structural distortion characterized by two distinct bond lengths between the center B-site cations and the Cl atom: $d_1(\mathrm{In}-\mathrm{Cl}) = 2.54\,\text{Å}$ and $d_2(\mathrm{Ag}-\mathrm{Cl}) = 2.66\,\text{Å}$. We also calculated the charge transfer between B-Cl (B = In, Ag) pairs using Bader analysis, as shown in Fig. 1(c). The results indicate a substantially greater electron loss from In atom (1.33e) compared to Ag atom (0.57e), reflecting bond strength disparity and consequent structural distortion. To investigate the chemical bonding features of $Cs_2AgInCl_6$, we plotted the electron localization function (ELF), as shown in Fig. 1(d). The results reveal pronounced covalent character in the In–Cl interactions. However, the charge density around Cs and Ag atoms is more localized. Specifically, the disparity between Ag–Cl and In–Cl pairs induces structural variations between $[AgCl_6]$ and $[InCl_6]$ octahedra, a feature typically associated with significant lattice anharmonicity.[19,39–41]

The temperature-dependent phonon dispersion characteristics are illustrated in Fig. 1(e). The 10-atom unit cell yields 3 acoustic and 27 optical branches. The absence of imaginary frequencies confirms dynamic stability. A pronounced stiffening is observed across the majority of the phonon spectrum as temperature increases, which is further corroborated by the atom-projected phonon density of states (PDOS) at 0, 300, and 500 K [Fig. 1(f)]. The temperature-induced frequency shift strengthens phonon interactions and modestly enhances phonon scattering. As a result, the calculated thermal conductivity values decrease marginally when temperature effects are included. Additionally, the calculated elastic constants (Table S1 of the SM) satisfy elastic stability criteria for cubic crystals ($C_{11} > C_{12}$, $C_{11} + 2C_{12} > 0$, and $C_{44} > 0$), confirming the mechanical stability of $Cs_2AgInCl_6$ at ambient pressure.

Figure 1(f) shows that the high-frequency (13–36 meV) optical branches primarily originate from the vibrations of In and Cl atoms, while the mid-frequency (9–12 meV) optical branches involve Ag and Cl atoms. The acoustic and low-frequency optical branches are dominated by Cs and Cl atoms between 5 and 8 meV. Vibrations of Cl atoms span the entire frequency range, indicating the delocalized bonding of Cl atoms with other atoms. Conversely, Cs atoms exhibit highly localized vibrations, stemming from flat-band optical phonons observed in the low-frequency region. The high PDOS of these flat bands [Fig. 1(e)] implies a high density of phonon modes within narrow energy ranges, promoting phonon emission and absorption, and increasing scattering probability.

Figure 1(g) highlights the avoided crossing interactions between the acoustic and low-frequency optical branches (black circles). This behavior induces strong phonon–phonon interactions between heat-carrying acoustic and low-frequency optical phonon modes, while the flat bands provide an extensive scattering phase space,[42–44] collectively diminishing phonon lifetimes and group velocities to suppress lattice thermal transport.

To comprehensively understand the thermal transport characteristics of $Cs_2AgInCl_6$, we calculated the unified κ_l within the framework of the Wigner formalism.[31] Figures 2(a) and 2(b) show the temperature dependence of κ_l for $Cs_2AgInCl_6$ from 300 to 700 K. At 300 K, when only 3ph scattering is considered [Fig. 2(a)], the particle-like phonon contribution κ_p is 0.46 $\mathrm{W\cdot m^{-1}\cdot K^{-1}}$,

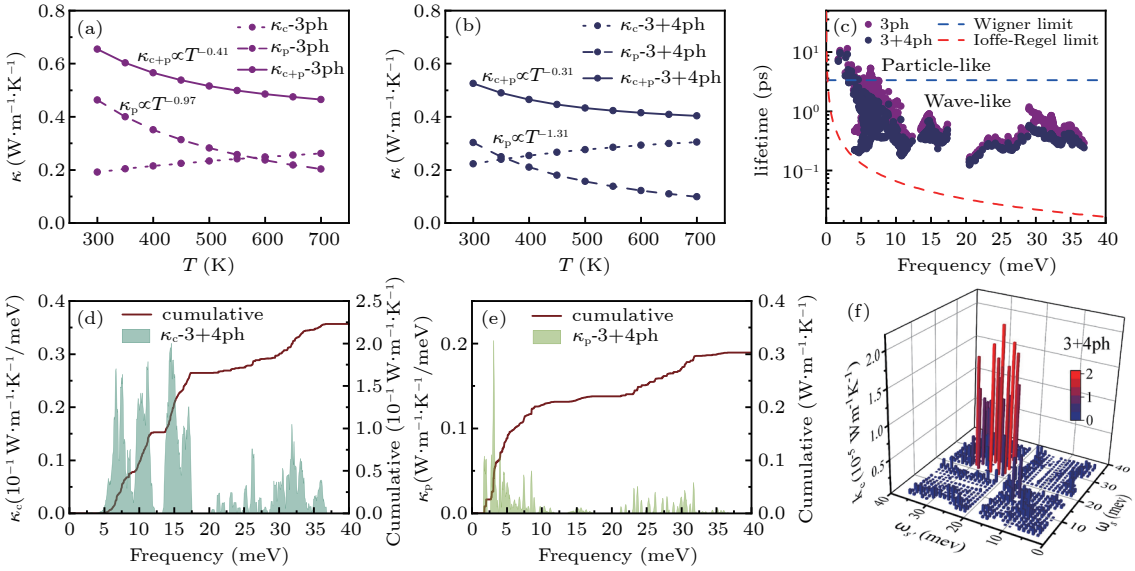

Fig. 2. Calculated temperature-dependent contributions to lattice thermal conductivity, including wave-like (κ_c), particle-like (κ_p), and total ($\kappa_c+\kappa_p$) components, considering (a) 3ph scattering and (b) combined 3+4ph scattering. (c) Comparison of phonon lifetimes under 3ph and 3+4ph scattering at 300 K. The blue dashed line denotes the Wigner limit. The red dashed line represents the Ioffe–Regel limit. Spectral and cumulative contributions to (d) κ_c and (e) κ_p under 3+4ph scattering as a function of phonon frequency at 300 K. (f) Three-dimensional stacked bar plots illustrating the off-diagonal contributions to κ_l from various phonon frequency pairs (ω_s and $\omega_{s'}$).

while the glass-like contribution κ_c is $0.19\,W{\cdot}m^{-1}{\cdot}K^{-1}$. Including 4ph processes, as shown in Fig. 2(b), κ_p decreases to $0.30\,W{\cdot}m^{-1}{\cdot}K^{-1}$, while κ_c increases slightly to $0.22\,W{\cdot}m^{-1}{\cdot}K^{-1}$, yielding a total κ_l of $0.52\,W{\cdot}m^{-1}{\cdot}K^{-1}$. This value is lower than typical thermoelectric materials like SnSe ($0.67\,W{\cdot}m^{-1}{\cdot}K^{-1}$)[45] and PbTe ($\sim 2.00\,W{\cdot}m^{-1}{\cdot}K^{-1}$),[46] and comparable to recently reported lead-free halide perovskites such as $CsNaInCl_6$ ($0.43\,W{\cdot}m^{-1}{\cdot}K^{-1}$)[15] and $Cs_3Bi_2Br_9$ ($0.40\,W{\cdot}m^{-1}{\cdot}K^{-1}$).[47] The 35% reduction in κ_p indicates significant 4ph scattering in $Cs_2AgInCl_6$. The κ_c contribution accounts for 42% of the total κ_l at 300 K, suggesting that $Cs_2AgInCl_6$ exhibits glass-like thermal transport behavior. To explore the role of glass-like thermal transport behavior, we further calculated the relationship $\kappa_l \propto T^{-\alpha}$ to examine the temperature dependence of κ_l. Initially, we analyze the temperature dependence of κ_p, which aligns closely with the standard $\alpha = 1$ for 3ph scattering. However, introducing the wave-like contribution κ_c results in $\alpha = 0.41$. When incorporating 4ph scattering, the temperature sensitivity of κ_l was further diminished to $\alpha = 0.31$. Thus, wave-like tunneling and 4ph scattering synergistically lower κ_l and weaken its temperature sensitivity.

To investigate the 4ph scattering and wave-like phonon tunneling in $Cs_2AgInCl_6$, we computed the 3ph and 3+4ph lifetimes across the entire frequency spectrum at 300 K, as illustrated in Fig. 2(c). Following the innovative concept introduced by Simoncelli *et al.*,[30,31] we distinguish the thermal transport regimes using the Wigner limit (τ_{Wigner}) and Ioffe–Regel limit ($\tau_{Ioffe-Regel}$) between particle-like propagation and wave-like tunneling behaviors. τ_{Wigner} is shown as the blue horizontal line in Fig. 2(c), which is defined as $\tau_{Wigner} = 1/\Delta\omega_{avg} = 3N_{at}/\omega_{max}$, where $\Delta\omega_{avg}$ represents the average interband spacing, N_{at} is the number of atoms in the primitive cell, and ω_{max} denotes the maximum phonon frequency. The red dashed line represents $\tau_{Ioffe-Regel} = 1/\omega$. Phonons with lifetimes $\tau > \tau_{Wigner}$ predominantly contribute to κ_p through particle-like propagation, whereas those with $\tau_{Ioffe-Regel} < \tau < \tau_{Wigner}$ engage in wave-like tunneling and drive the coherent contribution κ_c. Phonons with $\tau < \tau_{Ioffe-Regel}$ are overdamped characteristics and require spectral-function methodologies for accurate description.[48] Our results reveal that, whether including 4ph scattering processes, the majority of phonons possess lifetimes below τ_{Wigner}, underscoring the critical role of wave-like tunneling in thermal transport. Notably, incorporating 4ph scattering processes shortens phonon lifetimes, further suppresses κ_p, and enhances κ_c.[49] Furthermore, acoustic phonons with longer lifetimes in the particle-like region remain the main carriers in κ_p, while optical phonons with lifetimes concentrated in the wave-like regime are the primary contributors to κ_c.

These findings are further supported by the cumulative and differential spectra of κ_c and κ_p at 300 K, as shown in Figs. 2(d) and 2(e). The wave-like contribution κ_c arises from a broad range of phonon frequencies but is dominated by flat optical phonons. In contrast, the particle-like contribution κ_p is carried by acoustic phonons. To gain an intuitive understanding of the coherent contributions to thermal transport, we plotted three-dimensional visualizations of κ_c at 300 K, incorporating diverse phonon pair interactions, as depicted in Fig. 2(f). Consistent with prior analysis, optical phonon branches emerge as the primary contributors of κ_c. Notably, the phonon pairs exhibiting the strongest contributions to κ_c are predominantly located in the quasi-diagonal regions due to the smaller energy difference between eigenstates, with additional contributions from high-frequency non-diagonal pairs.

The above analyses explicitly demonstrate that decreased κ_l stems from enhanced phonon scattering rates, particularly the 4ph processes. The phonon scattering rate relies on the phase space. Therefore, we calculated the 3ph and 4ph scattering phase spaces contributed by different types of processes, as illustrated in Figs. 3(a) and 3(b). Figure 3(a) presents a decomposition of the phase space for 3ph interactions, including both absorption and emission processes. In the low-frequency regime, two low-energy phonons tend to merge into a single higher-energy phonon; while at higher frequencies, phonons are more prone to split into two lower-energy modes. This behavior strictly adheres to energy and momentum conservation principles. For 4ph scattering, we decompose the interactions into three distinct mechanisms: recombination, redistribution, and splitting, as shown in Fig. 3(b). Among these, redistribution processes dominate 4ph scattering due to the relaxed energy conservation constraints imposed by the selection rules.[50] Notably, the peak region of the 4ph redistribution processes aligns closely with the flat-bands associated with rattling modes of Cl and Cs atoms. When the participating phonons lie on a flat branch, the energy conservation requirement is more readily satisfied due to the higher density of modes at the same energy. Consequently, the greater abundance of energy-matched phonon pairs significantly enhances phonon–phonon scattering. Similar rattling mode enhanced 4ph scattering occurs in crystalline $Cs_2AgBiBr_6$[19] and $Cu_{12}Sb_4S_{13}$ Tetrahedrites.[35]

Generally, flat-band phonons are closely related to weakly bound atoms that can randomly fluctuate as rattling atoms. To gain insight into atomic-level dynamics, we calculate the potential energy surface (PES) by off-centering the atoms relative to their equilibrium positions, as shown in Fig. 3(c). It is clear that Cs and Cl atoms are confined in a flat potential well, suggesting that they can easily rattle from their equilibrium positions under minimal perturbations. The shallow PES indicates weak bonding, which results in large atomic displacement parameters (ADPs).

To quantify these vibrational amplitudes in $Cs_2AgInCl_6$, we calculated the ADPs to measure the mean-square displacement of each atom about its equilibrium position. Larger ADPs imply a weak bonding and characteristic of rattling atoms. As shown in Fig. 3(d), the order of atomic ADPs in $Cs_2AgInCl_6$ is: ADP(Cl) > ADP(Cs) > ADP(Ag) > ADP(In). At 300 K, the ADPs of Cl and Cs atoms reached 0.034 and 0.024 $Å^2$, respectively. The large ADPs of Cl and Cs atoms indicate that they are loosely bound within the lattice, and their corresponding sublattices exhibit rattling behavior. In addition,

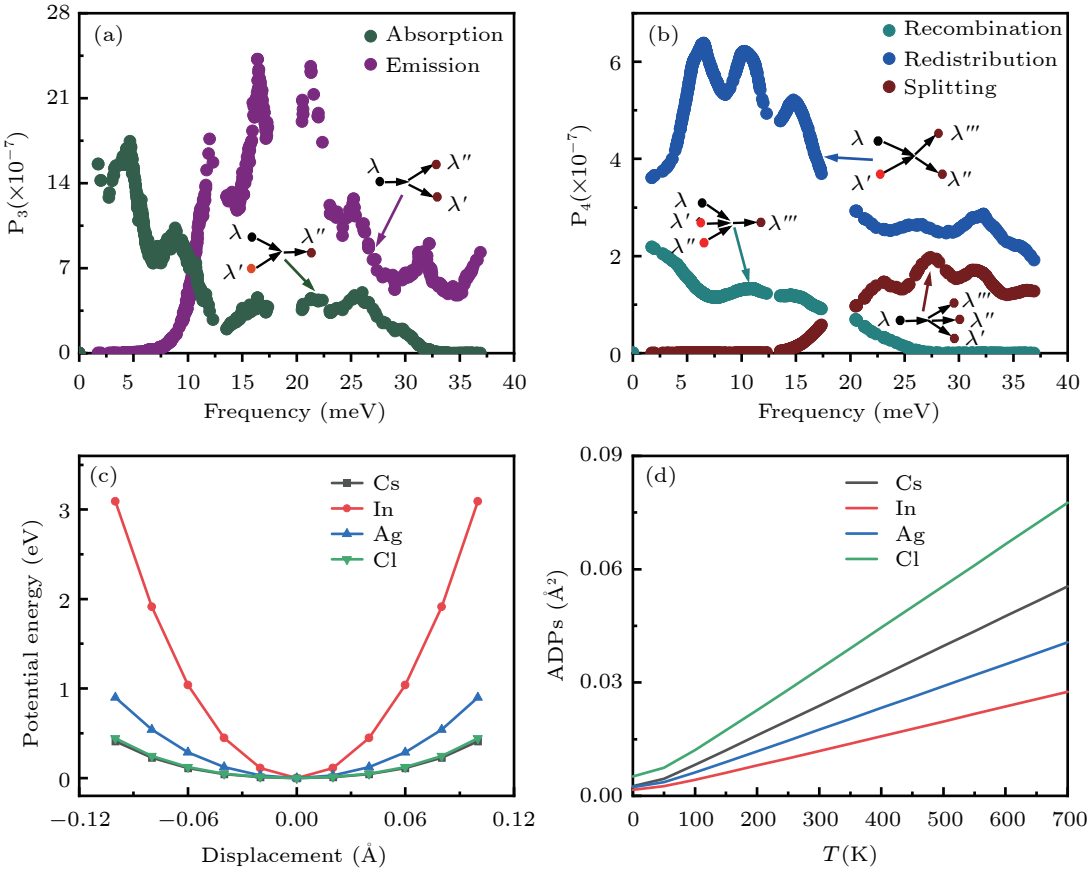

Fig. 3. (a) 3ph scattering phase space decomposed into the absorption ($\lambda + \lambda' \to \lambda''$), emission ($\lambda \to \lambda' + \lambda''$) processes. (b) 4ph scattering phase space resolved into recombination ($\lambda + \lambda' + \lambda'' \to \lambda'''$), redistribution ($\lambda + \lambda' \to \lambda'' + \lambda'''$), and splitting ($\lambda \to \lambda' + \lambda'' + \lambda'''$) processes of $Cs_2AgInCl_6$ at 300 K. (c) The potential energy and (d) ADPs for Cs, In, Ag, and Cl ions in $Cs_2AgInCl_6$.

we calculated the Lindemann parameter δ[49,51] for Cl and Cs atoms in $Cs_2AgInCl_6$, which are 0.042 and 0.072, respectively. The δ value of Cl approaches the melting Lindemann criterion of 0.07, suggesting that the sublattice of Cl atoms is near a liquid state. This implies that $Cs_2AgInCl_6$ exhibits coexisting crystalline and non-crystalline states, explaining its glass-like $\kappa_l \propto T^{-0.31}$.

As previously discussed, Cl and Cs collective motions dominate acoustic and low-frequency optical modes. These modes exhibit avoided crossings, which effectively suppress phonon group velocities (see Fig. S1 of the SM) and significantly enhance lattice anharmonicity (see Fig. S2 of the SM). Notably, large negative Grüneisen parameters γ in the acoustic and low-frequency optical modes below 5 meV play a dominant role in suppressing κ_p, owing to its inverse proportionality to γ^2.[52] The γ projected onto the phonon dispersion and the eigenvector of the lowest-frequency optical mode [Figs. S3(a) and S3(b) of the SM] reveal that Cl atoms form a large "rattling" cluster during vibrations. The relatively large atomic mass of Cl yields lower-frequency optical modes that are highly anharmonic.[41,53,54] It can be concluded that the glass-like behavior is one of the origins of the high anharmonicity in $Cs_2AgInCl_6$, thus giving rise to its low thermal conductivity. This pronounced anharmonicity arises from the hierarchy of bond strengths, as detailed in Figs. S4(a) and S4(b) and the accompanying analysis in the SM.

In summary, we have conducted a theoretical study on the crystal lattice and thermal transport properties of lead-free HDPs $Cs_2AgInCl_6$. Our calculations indicate that $Cs_2AgInCl_6$ exhibits ultralow κ_l of 0.52 $W{\cdot}m^{-1}{\cdot}K^{-1}$ at 300 K and a glassy temperature dependence of $T^{-0.31}$. We reveal that the presence of antibonding states gives rise to a strong chemical bond hierarchy associated with the weak bonding and flat phonon modes of rattling Cs and Cl atoms. Specifically, the vibrational modes associated with the sublattice of Cl atoms induce a mixed crystalline-liquid state in $Cs_2AgInCl_6$. The dynamic rotation of halogen atoms plays an important role in enhancing the lattice anharmonicity and limiting the thermal transport. In addition, 4ph scattering and the wave-like tunneling channel significantly modify the temperature dependence of κ_l. Our work contributes to a better understanding of the glass-like thermal transport in halide perovskites, which could be useful in thermoelectric applications.

Acknowledgements. This work was supported by the National Natural Science Foundation of China (Grant No. 12204482), the Natural Science Foundation of Shanxi Province (Grant No. 202403021221164), Higher education teaching reform and innovation project of Shanxi Province (Grant No. J20220480), and the Natural Science

Foundation of Hainan Province (Grant Nos. 525MS080 and 225MS076).

References

[1] He J and Tritt T M 2017 *Science* **357** eaak9997
[2] Stopyra M, Moskal G, Mikuśkiewicz M, and Fabrichnaya O 2024 *J. Eur. Ceram. Soc.* **44** 5129
[3] Zhao K P, Qiu P F, Shi X, and Chen L D 2019 *Adv. Funct. Mater.* **30** 1903867
[4] Cheng S J, Guo X X, Cai W W, Zhang Y F, and Zhang X A 2024 *J. Mater. Chem. A* **12** 8640
[5] Wu G J, Cai J F, Chen L D, Guo Z, Chen K Y, Tan X J, Wu J H, Liu G Q, and Jiang J 2024 *Adv. Funct. Mater.* **34** 2407818
[6] Chen C, Shen D Y, Xia C L, Zhang Z W, Wang W X, Zhang Q, and Chen Y 2022 *Chem. Eng. J.* **441** 135968
[7] Deng H Q, Lou X N, Lu W Q, Zhang J, Li D, Li S, Zhang Q T, Zhang X M, Chen X, Zhang D W, Zhang Y S, and Tang G D 2021 *Nano Energy* **81** 105649
[8] Chen C, Feng Z Z, Yao H H, Cao F, Lei B H, Wang Y M, Chen Y, Singh D J, and Zhang Q 2021 *Nat. Commun.* **12** 5718
[9] Dong L, Liu B H, Wang Y Y, and Xu X F 2022 *Chin. Phys. Lett.* **39** 127201
[10] Wu Y Q, Wei S F, Abdulkarim S, Shang Y, Wang J J, and Sun M T 2024 *Nano Lett.* **24** 11090
[11] Zhang Q H, Ai X, Wang L J, Chang Y X, Luo W, Jiang W, and Chen L D 2014 *Adv. Funct. Mater.* **25** 966
[12] Li M L, Shakoori M A, Wang R P, and Li H P 2024 *Chin. Phys. Lett.* **41** 016302
[13] Zheng B W, Chen T, Sun H R, Yang M M, Yang B C, Chen X, Zhang Y S, and Liu X B 2024 *Chin. Phys. Lett.* **41** 057301
[14] Cappai A, Melis C, Marongiu D, Quochi F, Saba M, Congiu F, He Y, Slade T J, Kanatzidis M G, and Colombo L 2024 *Adv. Sci.* **11** 2305861
[15] Wang G, Zheng J Z, Xue J, Xu Y X, Zheng Q Y, Hautier G, Lu H P, and Zhou Y G 2025 *Adv. Sci.* **12** 2408149
[16] Yan L F, Zhao L L, Zhao C Y, and Lin S C 2022 *Appl. Therm. Eng.* **215** 119024
[17] Lei H W, Hardy D, and Gao F 2021 *Adv. Funct. Mater.* **31** 2105898
[18] Yin H, Xian Y, Zhang Y, Chen W, Wen X, Rahman N U, Long Y, Jia B, Fan J, and Li W 2020 *Adv. Funct. Mater.* **30** 2002225
[19] Zheng J, Lin C, Lin C, Hautier G, Guo R, and Huang B 2024 *npj Comput. Mater.* **10** 30
[20] Volonakis G, Haghighirad A A, Milot R L, Sio W H, Filip M R, Wenger B, Johnston M B, Herz L M, Snaith H J, and Giustino F 2017 *J. Phys. Chem. Lett.* **8** 772
[21] Jebnouni A, Alatawi A A, Bouzidi M, Alshammari A F, Aljaloud A S, Alshammari M A F, Jebali M, and Bechir M B 2025 *Appl. Organomet. Chem.* **39** e8000
[22] Kresse G and Furthmuller J 1996 *Comp. Mater. Sci.* **6** 15
[23] Perdew J P, Ruzsinszky A, Csonka G I, Vydrov O A, Scuseria G E, Constantin L A, Zhou X, and Burke K 2008 *Phys. Rev. Lett.* **100** 136406
[24] John P P, Kieron B, and Matthias E 1996 *Phys. Rev. Lett.* **77** 3865
[25] Omini M and Sparavigna A 1996 *Phys. Rev. B* **53** 9064
[26] Zhou F, Nielson W, Xia Y, and Ozoliņš V 2019 *Phys. Rev. B* **100** 184308
[27] Ji L X, Huang A Q, Huo Y Q, Ding Y M, Zeng S M, Wu Y, and Zhou L J 2024 *Phys. Rev. B* **109** 214307
[28] Li W, Carrete J, A. Katcho N, and Mingo N 2014 *Comput. Phys. Commun.* **185** 1747
[29] Caldarelli G, Simoncelli M, Marzari N, Mauri F, and Benfatto L 2022 *Phys. Rev. B* **106** 024312
[30] Simoncelli M, Marzari N, and Mauri F 2022 *Phys. Rev. X* **12** 041011
[31] Simoncelli M, Marzari N, and Mauri F 2019 *Nat. Phys.* **15** 809
[32] Allen P B and Feldman J L 1989 *Phys. Rev. Lett.* **62** 645
[33] Tadano T and Saidi W A 2022 *Phys. Rev. Lett.* **129** 185901
[34] Xia Y, Pal K, He J, Ozoliņš V, and Wolverton C 2020 *Phys. Rev. Lett.* **124** 065901
[35] Xia Y, Ozolins V, and Wolverton C 2020 *Phys. Rev. Lett.* **125** 085901
[36] Ha V A, Volonakis G, Lee H, Zacharias M, and Giustino F 2021 *J. Phys. Chem. C* **125** 21689
[37] Akkerman Q A and Manna L 2020 *ACS Energy Lett.* **5** 604
[38] Momma K and Izumi F 2011 *J. Appl. Crystallogr.* **44** 1272
[39] Xie H Y and Zhao L D 2024 *Mater. Futures* **3** 013501
[40] Wu Y, Chen Y, Fang Z X, Ding Y M, Li Q Q, Xue K, Shao H Z, Zhang H, and Zhou L J 2023 *J. Phys. Chem. Lett.* **14** 11465
[41] Wu Y, Ji J L, Ding Y M, Yang J, and Zhou L J 2024 *Adv. Sci.* **11** 2406380
[42] Li H C, Yang Y, Xia Z H, Wang Y T, Wei J C, He J G, and Wang R M 2025 *Phys. Rev. B* **111** 125411
[43] Li W and Mingo N 2015 *Phys. Rev. B* **91** 144304
[44] Xie L, Feng J H, Li R, and He J Q 2020 *Phys. Rev. Lett.* **125** 245901
[45] Zhao L D, Lo S H, Zhang Y, Sun H, Tan G, Uher C, Wolverton C, Dravid V P, and Kanatzidis M G 2014 *Nature* **508** 373
[46] Tian Z, Garg J, Esfarjani K, Shiga T, Shiomi J, and Chen G 2012 *Phys. Rev. B* **85** 184303
[47] Ma J J, Zheng J J, Chen Y, Ren Q, Zhang J, and Wang B T 2024 *Phys. Chem. Chem. Phys.* **26** 21801
[48] Dangić D, Hellman O, Fahy S, and Savić I 2021 *npj Comput. Mater.* **7** 57
[49] Li J Y, Wei L M, Ti Z Y, Ma L, Yan Y L, Zhang G B, and Liu P F 2023 *Phys. Rev. B* **108** 224302
[50] Ravichandran N K and Broido D 2020 *Phys. Rev. X* **10** 021063
[51] Chakravarty C, Debenedetti P G, and Stillinger F H 2007 *J. Chem. Phys.* **126** 204508
[52] Morelli D T, Jovovic V, and Heremans J P 2008 *Phys. Rev. Lett.* **101** 035901
[53] Acharyya P, Ghosh T, Pal K, Kundu K, Singh Rana K, Pandey J, Soni A, Waghmare U V, and Biswas K 2020 *J. Am. Chem. Soc.* **142** 15595
[54] Ji J L, Liu Z H, Dai J H, Qiu D, Yang J, Xi J Y, Long Y W, and Zhang W Q 2023 *Mat. Today Phys.* **32** 101005